

# Preserve and Sculpt: Manifold-Aligned Fine-tuning of Vision-Language Models for Few-Shot Learning

Dexia Chen<sup>1</sup>, Qianjie Zhu<sup>2</sup>, Weibing Li<sup>1</sup>, Yue Yu<sup>3</sup>, Tong Zhang<sup>3</sup>, Ruixuan Wang<sup>1</sup>

<sup>1</sup>School of Computer Science and Engineering, Sun Yat-sen University, Guangzhou, China

<sup>2</sup>School of Computer, Electronics and Information, Guangxi University, Nanning, China

<sup>3</sup>Peng Cheng Laboratory, Shenzhen, China

{chendx27, liwb53, wangruix5}@mail.sysu.edu.cn, 2313394044@st.gxu.edu.cn, {yuy, zhangt02}@pcl.ac.cn

## Abstract

Pretrained vision-language models (VLMs), such as CLIP, have shown remarkable potential in few-shot image classification and led to numerous effective transfer learning strategies. These methods leverage the pretrained knowledge of VLMs to enable effective domain adaptation while mitigating overfitting through parameter-efficient tuning or instance-based consistency constraints. However, such regularizations often neglect the geometric structure of data distribution, which may lead to distortion of the overall semantic representation. To overcome this limitation, we propose a novel fine-tuning method, **Manifold-Preserving and Sculpting Tuning (MPS-Tuning)**. Regarding the data distribution in feature space as a semantic manifold, MPS-Tuning explicitly constrains the intrinsic geometry of this manifold while further sculpting it to enhance class separability. Specifically, MPS-Tuning preserves both macroscopic and microscopic topological structures of the original manifold by aligning Gram matrices of features before and after fine-tuning. Theoretically, this constraint is shown to approximate an upper bound of the Gromov-Wasserstein distance. Furthermore, features from the image and text modalities are paired, and pairwise similarities are optimized to enhance the manifold’s class discriminability. Extensive experiments demonstrate that MPS-Tuning significantly improves model performance while effectively preserving the structure of the semantic manifold. The code will be released.

## Introduction

Vision-language models (VLMs), exemplified by CLIP (Radford et al. 2021), have made significant progress by training on massive image-text pairs using contrastive learning. These models create joint embedding spaces where images and texts with similar meanings are well aligned. A compelling example is how the visual representation of a “cat” becomes positioned near the textual representation of “feline” but far from semantically distant concepts like “truck”. This intuitive structure of the embedding space directly contributes to the models’ exceptional ability to generalize across diverse tasks.

However, preserving this intricate semantic structure presents significant challenges during task adaptation, especially in few-shot learning scenarios. Standard fine-tuning approaches exhibit a tendency toward semantic structure collapse, where limited training samples cause catastrophic

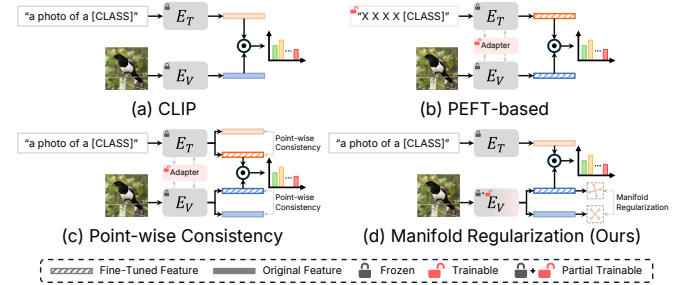


Figure 1: Comparison of regularization paradigms for VLMs. Previous fine-tuning methods (b, c) primarily constrain the number of tunable parameters or apply point-wise consistency constraints, potentially limiting the model’s learning capacity while neglecting the complete semantic manifold structure. In contrast, our method explicitly preserves the semantic manifold structure, significantly enhancing both generalization and learning capabilities.

forgetting of pre-trained representations, ultimately manifesting as severe degradation in generalization performance.

To address these challenges, two main paradigms of approaches have been proposed (Fig. 1). The first paradigm encompasses parameter-efficient fine-tuning (PEFT) methods, including prompt-based techniques such as CoOp (Zhou et al. 2022b) and adapter-based frameworks like CLIP-Adapter (Gao et al. 2024a), which mitigate overfitting by constraining the number of trainable parameters. The second paradigm comprises consistency-driven approaches, such as PromptSRC (Khattak et al. 2023b), which enforce consistency between the features or logits of individual samples before and after fine-tuning. Despite the demonstrated efficacy of these approaches, they either rely on implicit regularization of few-parameter fine-tuning, which limits model flexibility, or restrict variations in individual sample representations, which neglects the preservation of pretrained model’s semantic structure.

In contrast to existing methods that treat image data as isolated points, we propose Manifold-Preserving and Sculpting Tuning (MPS-Tuning), which views data distribution in the feature spaces as continuous semantic manifold, and aims to enhance its discrimination for downstream tasks while maintaining the intrinsic manifold structure. To preserve the

manifold structure, we constrain the Gromov-Wasserstein (GW) distance (Mémoli 2011) between the semantic manifolds derived from the features distributions of the fine-tuned and original models during training. Since directly computing GW distance is NP-hard and impractical for optimization, we simplify this problem and theoretically prove that the  $L_p$ -norm of the difference between corresponding Gram matrices provides an upper bound approximation to the GW distance of order  $p$ . Based on this theoretical insight, we propose Manifold Alignment Regularization, which preserves global topological structure via batch-level Gram matrices and maintains local geometric structure through token-level Gram matrices. For manifold sculpting, we introduce Hierarchical Manifold Sculpting with a multimodal query-support matching task, where each query achieves higher similarity with same-category pairs and lower similarity with different-category pairs. This sculpting mechanism is extended from the model’s output features to its intermediate layer features, further enhancing the discrimination of the manifold. Through manifold alignment and sculpting, robust adaptation of vision-language models is effectively achieved.

Our main contributions are summarized as follows:

- We propose a novel few-shot fine-tuning framework called MPS-Tuning, which enhances model performance while alleviating overfitting by explicitly aligning and sculpting the manifold geometry.
- We design a new regularization method, called Manifold Alignment Regularization, and establish its theoretical connection to the Gromov-Wasserstein distance for the first time, offering deeper insights into the preservation of manifold geometry.
- We introduce a hierarchical optimization strategy called Hierarchical Manifold Sculpting to actively enhance the discriminability of the manifold and further improve model performance.
- We evaluated the method’s performance on 11 datasets and conducted additional generalization evaluation on two datasets. Experimental results demonstrate that our method significantly outperforms current state-of-the-art approaches in few-shot image classification tasks.

## Related Work

### Vision-Language Models

In recent years, vision-language models (Radford et al. 2021; Sun et al. 2023; Xu et al. 2024; Gao et al. 2024b; Huang et al. 2024; Zhai et al. 2023; Tschannen et al. 2025; Pal et al. 2025) pretrained via contrastive learning on large-scale image-text pairs have demonstrated strong zero-shot generalization capabilities by aligning correctly matched images and texts. This enables them to be directly applied to various downstream tasks. Typically, such models consist of an image encoder  $E_V$  and a text encoder  $E_T$ . For a given classification task, text prompts (e.g., “a photo of a {class}”) are first constructed for each class, and a set of normalized class-specific textual features  $\{\mathbf{t}_1, \dots, \mathbf{t}_K\}$  is extracted using the text encoder  $E_T$ , where  $K$  denotes the number of

classes. Subsequently, for an input image  $\mathbf{x}$ , its normalized visual feature representation  $\mathbf{z}$  is obtained through the image encoder  $E_V$ . The probability of the image belonging to each class is then computed by applying the softmax function to the cosine similarities between  $\mathbf{z}$  and each class text feature  $\mathbf{t}_k$ , i.e.,

$$P(y = c_k | \mathbf{x}) = \frac{\exp(\langle \mathbf{z}, \mathbf{t}_k \rangle / \tau)}{\sum_{j=1}^K \exp(\langle \mathbf{z}, \mathbf{t}_j \rangle / \tau)}, \quad (1)$$

where  $\tau$  is a learnable temperature coefficient, and  $\langle \cdot, \cdot \rangle$  represents the inner product between two vectors. The model’s final prediction is given by the class with the highest probability, i.e.,

$$\hat{y} = \arg \max_{c_k \in \{c_1, \dots, c_K\}} P(y = c_k | x) \quad (2)$$

### Efficient Transfer Learning

To enable efficient adaptation of VLMs to downstream tasks while alleviating overfitting, a range of transfer learning strategies (Yang et al. 2024; Zhu et al. 2023; Xie et al. 2024; khattak et al. 2025; Guo et al. 2023; Zhu et al. 2024) have been proposed. These approaches can be grouped into two main paradigms. The first paradigm consists of PEFT-based methods that minimize computational overhead through targeted parameter updates. This includes prompt-based approaches that learn continuous, task-specific prompt vectors on the textual side, such as CoOp (Zhou et al. 2022b) and CoCoOp (Zhou et al. 2022a), and adapter-based methods, including CLIP-Adapter (Gao et al. 2024a), where visual features are refined via a lightweight adapter, and Tip-Adapter (Zhang et al. 2022), where classification is performed through the construction of a feature cache. The second paradigm is consistency-driven methods that incorporate consistency constraints to alleviate overfitting during fine-tuning. For example, PromptSRC (Khattak et al. 2023b) employs an L1 loss at the feature level and a KL divergence (Kullback and Leibler 1951) at the logit level to maintain pre-trained knowledge. While these methods demonstrate impressive performance on few-shot tasks, their flexibility is constrained by dependencies on PEFT strategies and point-based constraints. In contrast, our proposed manifold alignment regularization enables enhanced model adaptability while achieving superior preservation of pre-trained knowledge.

### Gromov-Wasserstein Distance

The Gromov-Wasserstein (GW) distance (Mémoli 2011) compares the intrinsic geometric structures of two metric spaces. Its core idea is to match the internal distance relationships between points rather than the points themselves. We consider two discrete metric spaces  $\mathbf{D}_X$  and  $\mathbf{D}_Y$ , and their associated probability distributions  $\mu$  and  $\nu$ . The GW distance seeks an optimal *coupling*  $\pi$ , which acts as a probabilistic transportation plan between the distributions  $\mu$  and  $\nu$ . The discrete GW distance is formally defined as:

$$GW_p(\mu, \nu) = \left( \min_{\pi \in \Pi(\mu, \nu)} \sum_{i,j=1}^n \sum_{k,l=1}^m |(\mathbf{D}_X)_{ij} - (\mathbf{D}_Y)_{kl}|^p \pi_{ik} \pi_{jl} \right)^{1/p} \quad (3)$$

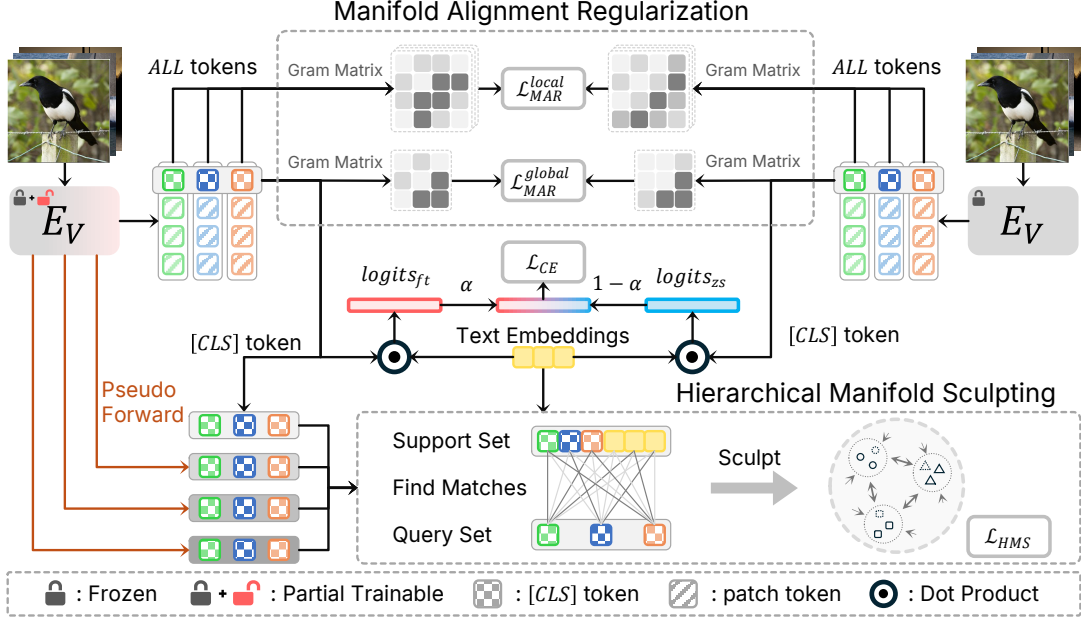


Figure 2: Overview of the MPS-Tuning, which integrates Manifold Alignment Regularization and Hierarchical Manifold Sculpting. Manifold Alignment Regularization prevents knowledge degradation by aligning Gram matrices across fine-tuned and original CLIPs at both global and local scales. Hierarchical Manifold Sculpting enhances local manifold adaptability via query-support matching, tailoring representations to downstream tasks. Through Pseudo Forward, this sculpting process extends to intermediate layers, ensuring effective semantic-task manifold alignment.  $E_V$  represents the visual encoder.

This formula minimizes the expected  $p$ -power difference between pairwise distances in the two spaces, under the optimal coupling  $\pi$ . By focusing on the similarity of distance matrices rather than direct point correspondence, GW distance effectively captures geometric structures. However, finding the optimal coupling  $\pi$  is a quadratic assignment problem, which is NP-hard and thus computationally intractable for high-dimensional data. To address this, we adopt a fixed coupling scheme, which provides a tractable upper bound on the GW distance and transforms it into a computationally feasible regularization. To the best of our knowledge, this work represents the first application of GW distance theory to VLM fine-tuning, offering a principled approach to preserving geometric knowledge in pretrained models. More details are in Appendix A.

## Method

To facilitate effective downstream adaptation without disrupting the inherent structure of the pre-trained representation manifold, we propose a novel approach termed Manifold-Preserving and Sculpting Tuning (MPS-Tuning). This method employs Manifold Alignment Regularization (MAR) to prevent drastic alterations in the semantic structure of feature manifold and incorporates Hierarchical Manifold Sculpting (HMS) to progressively refine local manifold structures. Specifically, MAR aligns the Gram matrices of the fine-tuned and the original models at both the batch and token levels, thereby maintaining consistency in semantic geometry and mitigating overfitting risks. In paral-

lel, HMS refines local manifold structures by performing a multimodal query-support matching task between image and text representations, optimizing similarity at both intermediate and output feature levels. This results in more compact intra-class clusters and better separated inter-class distributions. By jointly applying MAR and HMS, MPS-Tuning achieves robust and efficient adaptation to new tasks, maintaining the valuable structural knowledge of the pre-trained model and demonstrating strong performance in few-shot learning scenarios.

### Manifold Alignment Regularization

The feature distribution learned by a pre-trained model can be regarded as a well-structured semantic manifold, whose geometric structure encodes rich prior knowledge. Preserving this geometric structure allows for the retention of more comprehensive pre-trained knowledge. To this end, we propose Manifold Alignment Regularization (MAR), which enforces alignment between the geometric structures of feature manifolds before and after fine-tuning, thereby enhancing model performance.

As a metric designed to quantify the similarity between different metric spaces, the Gromov-Wasserstein (GW) distance serves as a powerful tool for evaluating changes in the structure of feature manifolds induced by model fine-tuning. Our MAR provides an efficient upper-bound approximation to the GW distance. To formally justify this approximation, we present the following theorem:

**Theorem 1** *The alignment of the Gram matrices under the*

$L_p$ -norm serves as an approximate upper bound of the  $p$ -order Gromov-Wasserstein distance.

**Proof Outline.** We consider the feature spaces of the original CLIP model and the fine-tuned CLIP model as two metric spaces. By fixing a natural coupling (i.e., assuming a one-to-one correspondence between features of the same sample across the two models), the NP-hard computation of the GW distance is reduced to an efficient upper-bound approximation. Specifically, the approximate upper bound of the discrete  $GW_p$  distance between the two metric spaces is given by the  $L_p$ -norm of the difference between their respective Gram matrices. Refer to Appendix A for the complete proof.

Guided by this theory, alignment regularizations are introduced at two distinct levels.

**Global topological alignment** To maintain the integrity of the global manifold structure, relational constraints among samples are enforced at the batch level. Given a mini-batch of  $N$  samples, we extract normalized [CLS] token features from the pre-trained model as  $\{\mathbf{z}_1, \dots, \mathbf{z}_N\} \in \mathbb{R}^{N \times d}$  and from the fine-tuned model as  $\{\mathbf{z}'_1, \dots, \mathbf{z}'_N\} \in \mathbb{R}^{N \times d}$ . The Gram matrices  $\mathbf{S}, \mathbf{S}' \in \mathbb{R}^{N \times N}$  are computed via inner products  $S_{ij} = \langle \mathbf{z}_i, \mathbf{z}_j \rangle$  and  $S'_{ij} = \langle \mathbf{z}'_i, \mathbf{z}'_j \rangle$ . The global topological alignment loss is defined as

$$\mathcal{L}_{\text{MAR}}^{\text{global}} = \frac{1}{N^2} \sum_{i=1}^N \sum_{j=1}^N |S_{ij} - S'_{ij}|_1. \quad (4)$$

**Local geometric alignment** To retain the internal geometric structure within individual samples, regularization is separately performed on the interactions between the [CLS] token and the patch tokens, as well as on the internal relations among the patch tokens. For the  $i$ -th sample, we collect features before fine-tuning as  $\{\mathbf{z}_{\text{cls}}^{(i)}, \mathbf{z}_1^{(i)}, \dots, \mathbf{z}_M^{(i)}\} \in \mathbb{R}^{(M+1) \times d}$  and after fine-tuning as  $\{\mathbf{z}'_{\text{cls}}^{(i)}, \mathbf{z}'_1^{(i)}, \dots, \mathbf{z}'_M^{(i)}\} \in \mathbb{R}^{(M+1) \times d}$ , where  $M$  denotes the number of patch tokens. The intra-sample Gram matrices  $\mathbf{S}_i^{\text{intra}}, \mathbf{S}_i'^{\text{intra}} \in \mathbb{R}^{(M+1) \times (M+1)}$  are computed using inner products among [CLS] and patch tokens. The local alignment loss is given by

$$\mathcal{L}_{\text{MAR}}^{\text{local}} = \frac{1}{N} \sum_{i=1}^N \left( \frac{1}{(M+1)^2} \sum_{k=0}^M \sum_{l=0}^M |S_{i,kl}^{\text{intra}} - S_{i,kl}'^{\text{intra}}|_1 \right). \quad (5)$$

The final manifold alignment regularization term is the sum of the above two terms, i.e.,

$$\mathcal{L}_{\text{MAR}} = \mathcal{L}_{\text{MAR}}^{\text{global}} + \mathcal{L}_{\text{MAR}}^{\text{local}}. \quad (6)$$

## Hierarchical Manifold Sculpting

To facilitate the acquisition of task-specific knowledge, we propose a hierarchical optimization of the local feature manifold. This process is formulated as a query-support matching task, which aims to encourage high similarity for positive image-text or image-image pairs and discourage incorrect matches. Let  $\mathcal{Q} = \{\mathbf{q}_1, \mathbf{q}_2, \dots, \mathbf{q}_N\}$  be the set of normalized image features used as queries, and let  $\mathcal{T} = \{\mathbf{t}_1, \mathbf{t}_2, \dots, \mathbf{t}_K\}$  be the set of frozen text embeddings. The

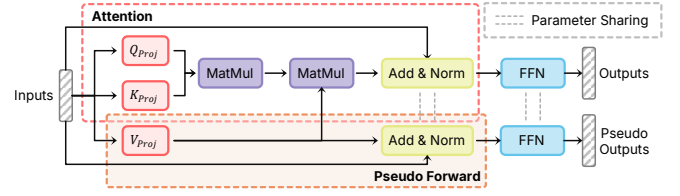


Figure 3: Pseudo-Forward projection bypass the attention allocation component in the model, and map intermediate layer features to the output feature space.

support set is then defined as the union  $\mathcal{S} = \mathcal{Q} \cup \mathcal{T}$ . Positive matches are defined based on category identity. Since limited batch sizes may lead to missing visual positives, data augmentation is applied to generate two augmented views per image, enriching the image pool. The task is optimized via a sculpting loss, which applies contrastive learning between each query and its positive matches:

$$\mathcal{L}_{\text{sculpt}}^{\text{query}}(\mathbf{q}, \mathcal{S}) = -\frac{1}{|\mathcal{P}_{\mathbf{q}}|} \sum_{\mathbf{s} \in \mathcal{P}_{\mathbf{q}}} \log \frac{\exp(\langle \mathbf{q}, \mathbf{s} \rangle) / \tau'}{\sum_{\mathbf{s}' \in \mathcal{S} \setminus \mathcal{P}_{\mathbf{q}}} \exp(\langle \mathbf{q}, \mathbf{s}' \rangle) / \tau'}, \quad (7)$$

where  $\tau'$  is a temperature factor and  $\mathcal{P}_{\mathbf{q}}$  represents the set of samples from  $\mathcal{S}$  that are positively paired with the query  $\mathbf{q}$ . The final objective over the batch is obtained by averaging this loss across all queries:

$$\mathcal{L}_{\text{sculpt}}(\mathcal{Q}, \mathcal{S}) = \mathbb{E}_{\mathbf{q} \in \mathcal{Q}} [\mathcal{L}_{\text{sculpt}}^{\text{query}}(\mathbf{q}, \mathcal{S})], \quad (8)$$

Furthermore, the manifold refinement is extended to intermediate transformer blocks to further sculpt the manifold. However, intermediate features  $\mathbf{z}'^{(l)}$  are not compatible with text embeddings. To address this issue, we implement a pseudo-forward projection (Fig. 3), skipping attention modules while retaining essential transformations in model, i.e.,

$$\hat{\mathbf{z}}'^{(l)} = \text{FFN}^{(L)} \circ V_{\text{Proj}}^{(L)} \circ \dots \circ \text{FFN}^{(l+1)} \circ V_{\text{Proj}}^{(l+1)}(\mathbf{z}'^{(l)}). \quad (9)$$

The overall HMS loss thus aggregates both final and intermediate layer alignment as follows,

$$\mathcal{L}_{\text{HMS}} = \mathcal{L}_{\text{sculpt}}(\hat{\mathcal{Q}}, \hat{\mathcal{S}}) + \sum_{l \in L_{\text{blocks}}} \mathcal{L}_{\text{sculpt}}(\mathcal{Q}^{(l)}, \mathcal{S}^{(l)}) \quad (10)$$

where  $\hat{\mathcal{Q}}, \hat{\mathcal{S}}$  are the output query and support sets,  $\mathcal{Q}^{(l)}, \mathcal{S}^{(l)}$  are their counterparts at layer  $l$  after pseudo forward projection, and  $L_{\text{blocks}}$  denotes the layer scope of HMS.

## Training and Inference

Leveraging the MPS-Tuning's strong knowledge retention capability, we can fine-tune partial model weights directly without causing overfitting, thereby substantially enhancing the model's learning capacity. See Appendix C for details.

The final logits for training and inference are a weighted sum of the fine-tuned and original model logits, i.e.,

$$\text{logits} = \alpha \cdot \text{logits}_{\text{ft}} + (1 - \alpha) \cdot \text{logits}_{\text{zs}}. \quad (11)$$

The total loss function for training combines the standard cross-entropy loss with our two regularization terms, i.e.,

$$\mathcal{L} = \mathcal{L}_{\text{CE}} + \lambda_1 \mathcal{L}_{\text{MAR}} + \lambda_2 \mathcal{L}_{\text{HMS}} \quad (12)$$

where  $\lambda_1$  and  $\lambda_2$  are hyperparameters that balance the contributions of the regularization terms.



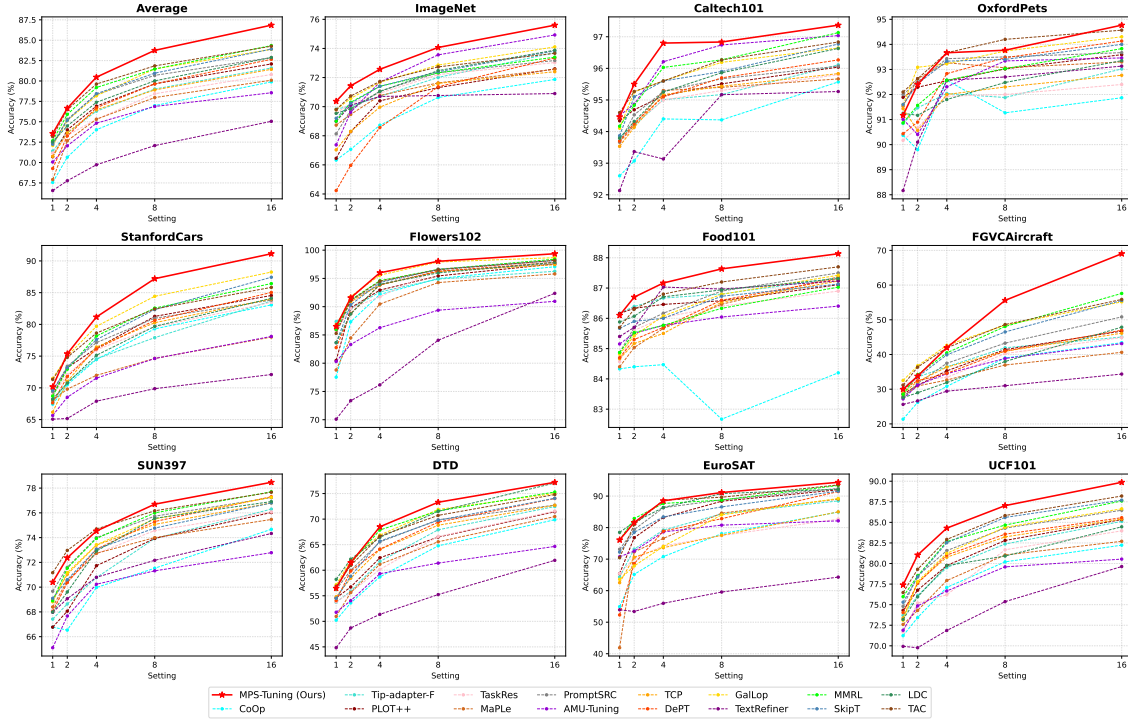


Figure 4: Performance comparison on 11 benchmark datasets.

## Experiments

### Experimental Settings

**Datasets** Following previous work (Zhou et al. 2022b; Yu et al. 2023), we evaluated our method on 11 datasets, including ImageNet (Deng et al. 2009), Caltech101 (Fei-Fei, Fergus, and Perona 2007), Food101 (Bossard, Guillaumin, and Gool 2014), DTD (Cimpoi et al. 2014), EuroSAT (Helber et al. 2019), FGVCAircraft (Maji et al. 2013), Flowers102 (Nilsback and Zisserman 2008), OxfordPets (Parkhi et al. 2012), StanfordCars (Krause et al. 2013), SUN397 (Xiao et al. 2010), and UCF101 (Soomro, Zamir, and Shah 2012). Additionally, domain generalization capabilities were further assessed using the ImageNet-Sketch (Wang et al. 2019) and ImageNet-V2 (Recht et al. 2019) datasets.

**Implementation** Following previous work (Zhou et al. 2022b; Yu et al. 2023), the model was trained on K-shot settings ( $K = 1, 2, 4, 8, 16$ ) and evaluated on the full test set using CLIP with ViT-B/16 (Dosovitskiy et al. 2021) and predefined text templates. Optimization was performed using SGD with cosine learning rate decay over 50 epochs, where a warm-up strategy increased the learning rate linearly from  $1e-5$  to 0.002 during the first epoch. Data augmentation strategies consistent with those used in CoOp, including random cropping and random flipping, were applied. For hyperparameter configuration, the weights for MAR ( $\lambda_1$ ), HMS ( $\lambda_2$ ) and logits weight ( $\alpha$ ) were set to 0.5, 0.1 and 0.3, respectively, with HMS applied to the last two layers. All results were averaged over three random seeds.

**Baselines** To demonstrate the superiority of our method, comprehensive comparisons were conducted against several SOTA methods, including CoOp (Zhou et al. 2022b), Tip-Adapter-F (Zhang et al. 2022), PLOT++ (Chen et al. 2023), MaPLe (Khattak et al. 2023a), PromptSRC (Khattak et al. 2023b), AMU-Tuning (Tang et al. 2024), TCP (Yao, Zhang, and Xu 2024), DePT (Zhang et al. 2024), Gallop (Lafon et al. 2024), TextRefiner (Xie et al. 2024), MMRL (Guo and Gu 2025), SkipT (Wu et al. 2025), LDC (Li et al. 2025), and TAC (Hao et al. 2025).

### Efficacy Study

**Classification Results** As shown in Fig. 4, our method achieves superior average performance across all shot settings compared to competing methods, with the performance gap widening as the number of training samples increases. Specifically, under the 1-shot, 4-shot, and 16-shot conditions, our approach improves accuracy by 0.88%, 1.27%, and 2.51%, respectively, over the strongest baseline. On natural image datasets such as ImageNet and SUN397, where the pre-trained CLIP model has already encoded rich visual knowledge, MAR facilitates the integration of downstream task learning while preserving this prior knowledge, leading to significant performance gains. For datasets with greater cross-domain challenges, such as StanfordCars, FGVCAircraft, and UCF101, the synergistic operation of HMS and MAR enables our method to effectively balance novel knowledge acquisition with pre-trained knowledge retention, yielding significant performance advantages.

**Domain Generalization Results** To validate the robust-

Table 1: Generalization results on ImageNet and its variants.

Method	Source	Target		Avg
	ImageNet	-Sketch	-V2	
CLIP	66.73	46.15	60.83	57.90
Linear Probe CLIP	65.85	34.77	56.26	52.29
CoOp	71.92	46.71	64.18	60.94
MaPLe	72.56	49.20	64.10	61.95
PromptSRC	73.17	49.10	65.70	62.66
TCP	72.40	48.17	64.83	61.80
MMRL	72.03	49.17	64.47	61.89
SkipT	72.77	49.73	65.67	62.72
MPS-Tuning (Ours)	<b>75.60</b>	<b>50.10</b>	<b>67.53</b>	<b>64.41</b>

Table 2: Efficiency comparison on SUN397.

Method	Training FPS	Inference FPS
CLIP	-	617
CoCoOp	4.20	13.0
TCP	120.9	617
TextRefiner	85.30	553
MPS-Tuning (Ours)	95.65	535

ness of MPS-Tuning, models were trained on the ImageNet dataset and subsequently evaluated on both ImageNet-V2 and ImageNet-Sketch datasets. As demonstrated in Tab. 1, MPS-Tuning consistently outperforms all baseline methods across the three datasets, thereby confirming its superior domain generalization capabilities.

**Efficiency** The training and inference FPS of MPS-Tuning were evaluated on the SUN397 dataset on a single RTX 3090 GPU to assess its efficiency. As shown in Tab. 2, the method demonstrates comparable efficiency to existing approaches.

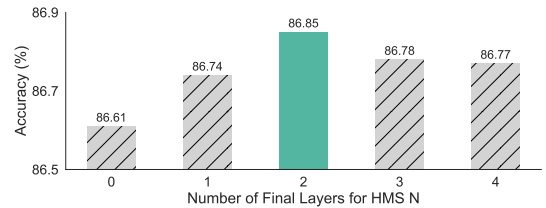
## Ablation Study

**Impact of Model Components** To establish the individual contribution of each proposed module, ablation studies were conducted on the ImageNet, StanfordCars, and SUN397 datasets under 16-shot settings. Tab. 3 illustrates that both modules contribute meaningful performance gains over the standard cross-entropy loss when applied separately, while their joint application achieves additional improvements.

**Impact of Global and Local Alignment** To assess the roles of global topological and local geometric alignment, we perform ablation studies under 1-shot, 4-shot, and 16-shot settings. As shown in Tab. 4, both alignments consistently improve performance, but exhibit different preferences across sample sizes. Global alignment is more beneficial in low-shot scenarios, while local alignment becomes more effective as sample size increases. This is because global alignment offers essential relational priors when the model lacks enough data to capture inter-class structure, whereas local alignment enhances robustness by preventing shortcut learning from incidental factors when more data is available. Combining both leads to the best performance, confirming their complementary nature at different structural levels.

Table 3: Ablation study on different components. “Avg11” is the average over all 11 benchmark datasets.

Components			Datasets			
$\mathcal{L}_{CE}$	$\mathcal{L}_{MAR}$	$\mathcal{L}_{HMS}$	ImageNet	Cars	SUN397	Avg11
✓			72.93	90.00	76.30	85.41
✓	✓		75.30	90.80	78.07	86.44
✓		✓	74.77	90.77	77.80	86.20
✓	✓	✓	<b>75.60</b>	<b>91.13</b>	<b>78.47</b>	<b>86.85</b>

Figure 5: Ablation study on HMS depth. The x-axis  $N$  means applying HMS to the last  $N$  layers of the model.

**Comparison to other Consistency Constraints** The effectiveness of MAR was further validated through performance comparisons with standard point-wise consistency constraints applied at feature and logit levels. As shown in Tab. 5, under 1-shot, 4-shot, and 16-shot settings, our method outperformed the strongest baselines by 0.64%, 0.74%, and 0.77% on ImageNet, and by 0.78%, 0.81%, and 0.61% when averaged across all 11 datasets. These results confirm that manifold-based consistency regularization yields superior performance improvements compared to point-alignment-based consistency constraints.

**Impact of HMS depth** The application scope of HMS was further explored. As shown in Fig. 5, applying HMS to final layer and penultimate layer yields the best performance gain, while extending it to earlier layers results in degradation. This finding aligns with the semantic hierarchy in neural networks (Zeiler 2014; Krizhevsky, Sutskever, and Hinton 2012; Gandelsman, Efros, and Steinhart 2024): deeper layers encode class-specific features that benefit from HMS, whereas intermediate layers capture more generic representations. Applying HMS too early may induce premature specialization, leading to overfitting. Therefore, HMS is used in the last two layers to enhance high-level representation learning while maintaining generalization.

## Interpretability Study

**Quantitative Analysis of Manifold Preservation** To further validate MAR’s manifold preservation capabilities, representational similarity analysis (Kriegeskorte, Mur, and Bandettini 2008) was applied to models before and after fine-tuning, enabling quantitative evaluation of semantic manifold structural variations. Fig. 6 shows that MAR achieves the best manifold structure preservation on natural image datasets like ImageNet and SUN397, where pre-trained CLIP already contains sufficient knowledge. Further-

Table 4: Ablation study on MAR. “Avg11” is the average over all 11 benchmark datasets.

Method	1-shot			4-shot			16-shot		
	ImageNet	UCF101	Avg11	ImageNet	UCF101	Avg11	ImageNet	UCF101	Avg11
None	69.33	76.73	72.35	71.57	83.63	79.60	74.77	89.23	86.20
only Global	70.03	77.37	73.42	72.23	83.90	80.18	75.17	89.53	86.57
only Local	69.90	76.73	72.82	72.43	84.27	80.21	75.57	89.60	86.67
MAR (Global+Local)	<b>70.37</b>	<b>77.40</b>	<b>73.55</b>	<b>72.57</b>	<b>84.30</b>	<b>80.47</b>	<b>75.60</b>	<b>89.87</b>	<b>86.85</b>

Table 5: Ablation study of different consistency constraints. “Avg11” is the average over all 11 benchmark datasets.

Consistency Constraint		1-shot			4-shot			16-shot		
		ImageNet	UCF101	Avg11	ImageNet	UCF101	Avg11	ImageNet	UCF101	Avg11
Feature-based	$\cos$	69.73	75.37	72.77	71.83	82.63	79.36	74.73	88.20	86.07
	$\ell_1$	69.43	76.73	72.41	71.63	83.63	79.66	74.83	89.23	86.24
	$\ell_2$	69.33	76.80	72.35	71.63	83.60	79.65	74.77	89.17	86.20
Logits-based	$kl$	69.67	73.00	71.43	71.60	78.70	77.77	73.87	84.97	84.20
	$\ell_1$	69.50	75.00	71.91	71.50	81.03	78.22	74.67	87.67	85.65
	$\ell_2$	69.47	74.93	71.85	71.57	81.10	77.51	74.70	87.73	85.59
Manifold-based	$\mathcal{L}_{MAR}$	<b>70.37</b>	<b>77.40</b>	<b>73.55</b>	<b>72.57</b>	<b>84.30</b>	<b>80.47</b>	<b>75.60</b>	<b>89.87</b>	<b>86.85</b>

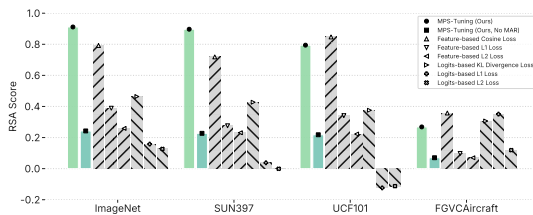


Figure 6: Representation similarity analysis of different consistency constraint mechanisms.

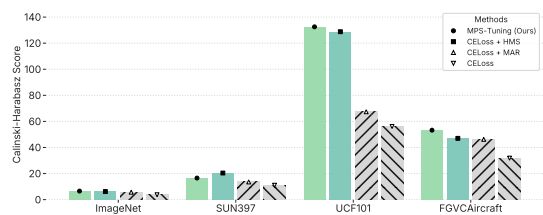


Figure 7: Class separability assessment of different component categories using Calinski-Harabasz score.

more, we find that MAR’s preservation capability spontaneously diminishes on datasets with extensive novel task-relevant knowledge (UCF101, FGVC Aircraft). This adaptive behavior results from MAR’s relaxed Gram matrix alignment rather than rigid feature or logits constraints, enabling knowledge preservation when beneficial while allowing adaptation when necessary. Additionally, we find that cosine similarity and KL divergence impose stricter manifold structure preservation compared to other point-based consistency constraints through their holistic vector-level restrictions, whereas L1 and L2 losses independently constrain each channel’s variation, potentially causing minimal per-channel changes but substantial overall vector modifications. However, their excessive strictness can limit learning (e.g., UCF101 and Avg11 results in Tab. 5), whereas MAR’s Gram matrix consistency provides dynamic constraints that balance preservation with learning capability.

**Quantitative Evaluation of Class Separation** To assess feature clustering behavior, we apply the Calinski-Harabasz Index (Calinski et al. 1974) on test sets from ImageNet, SUN397, UCF101 and FGVC Aircraft. As shown in Fig. 7, both HMS and MAR individually improve clustering per-

formance compared to cross-entropy loss, with HMS performing particularly well on cross-domain dataset UCF101. The combination of HMS and MAR yields similar scores to those of HMS alone, suggesting that our method effectively improves feature separability.

## Conclusion

In this study, we present MPS-Tuning, a novel manifold alignment-based fine-tuning framework that preserves the manifold structure of pre-trained models through Manifold Alignment Regularization while enhancing the discriminative capacity of semantic manifolds for downstream tasks via Hierarchical Manifold Sculpting. We provide theoretical validation by demonstrating that Manifold Alignment Regularization constitutes an approximate upper bound of the Gromov-Wasserstein distance, thereby establishing the theoretical foundation for its effectiveness. Extensive experiments demonstrate that MPS-Tuning significantly improves VLM performance in few-shot scenarios. This work introduces a novel perspective on VLM fine-tuning and shows promise for broader applicability across diverse scenarios.

## References

- Bossard, L.; Guillaumin, M.; and Gool, L. V. 2014. Food-101 - Mining Discriminative Components with Random Forests. In *ECCV*.
- Calinski, T.; Harabasz, and J. 1974. A Dendrite Method for Cluster Analysis. *Comm in Stats Simulation & Comp.*
- Chen, G.; Yao, W.; Song, X.; Li, X.; Rao, Y.; and Zhang, K. 2023. PLOT: Prompt Learning with Optimal Transport for Vision-Language Models. In *ICLR*.
- Cimpoi, M.; Maji, S.; Kokkinos, I.; Mohamed, S.; and Vedaldi, A. 2014. Describing Textures in the Wild. In *CVPR*.
- Deng, J.; Dong, W.; Socher, R.; Li, L.; Li, K.; and Fei-Fei, L. 2009. ImageNet: A large-scale hierarchical image database. In *CVPR*.
- Dosovitskiy, A.; Beyer, L.; Kolesnikov, A.; Weissenborn, D.; Zhai, X.; Unterthiner, T.; Dehghani, M.; Minderer, M.; Heigold, G.; Gelly, S.; Uszkoreit, J.; and Houslsby, N. 2021. An Image is Worth 16x16 Words: Transformers for Image Recognition at Scale. In *ICLR*.
- Fei-Fei, L.; Fergus, R.; and Perona, P. 2007. Learning generative visual models from few training examples: An incremental Bayesian approach tested on 101 object categories. *Comput. Vis. Image Underst.*, 106(1): 59–70.
- Gandelsman, Y.; Efros, A. A.; and Steinhardt, J. 2024. Interpreting CLIP’s Image Representation via Text-Based Decomposition. In *ICLR*.
- Gao, P.; Geng, S.; Zhang, R.; Ma, T.; Fang, R.; Zhang, Y.; Li, H.; and Qiao, Y. 2024a. Clip-adapter: Better vision-language models with feature adapters. *International Journal of Computer Vision*, 132(2): 581–595.
- Gao, Y.; Liu, J.; Xu, Z.; Wu, T.; Zhang, E.; Li, K.; Yang, J.; Liu, W.; and Sun, X. 2024b. Softclip: Softer cross-modal alignment makes clip stronger. In *AAAI*.
- Guo, Y.; and Gu, X. 2025. Mmrl: Multi-modal representation learning for vision-language models. In *CVPR*.
- Guo, Z.; Zhang, R.; Qiu, L.; Ma, X.; Miao, X.; He, X.; and Cui, B. 2023. CALIP: Zero-Shot Enhancement of CLIP with Parameter-Free Attention. In *AAAI*.
- Hao, F.; He, F.; Wu, F.; Wang, T.; Song, C.; and Cheng, J. 2025. Task-Aware Clustering for Prompting Vision-Language Models. In *CVPR*.
- Helber, P.; Bischke, B.; Dengel, A.; and Borth, D. 2019. EuroSAT: A Novel Dataset and Deep Learning Benchmark for Land Use and Land Cover Classification. *IEEE J. Sel. Top. Appl. Earth Obs. Remote. Sens.*, 12(7): 2217–2226.
- Huang, Y.; Tang, J.; Chen, Z.; Zhang, R.; Zhang, X.; Chen, W.; Zhao, Z.; Zhao, Z.; Lv, T.; Hu, Z.; and Zhang, W. 2024. Structure-CLIP: Towards Scene Graph Knowledge to Enhance Multi-modal Structured Representations. In *AAAI*.
- khattak, M. U.; Ferjad, M.; Muzzamal, N.; Gool, L. V.; and Tombari, F. 2025. Learning to Prompt with Text Only Supervision for Vision-Language Models. In *AAAI*.
- Khattak, M. U.; Rasheed, H. A.; Maaz, M.; Khan, S. H.; and Khan, F. S. 2023a. MaPLe: Multi-modal Prompt Learning. In *CVPR*.
- Khattak, M. U.; Wasim, S. T.; Naseer, M.; Khan, S.; Yang, M.-H.; and Khan, F. S. 2023b. Self-regulating prompts: Foundational model adaptation without forgetting. In *ICCV*.
- Krause, J.; Stark, M.; Deng, J.; and Fei-Fei, L. 2013. 3D Object Representations for Fine-Grained Categorization. In *ICCV*.
- Kriegeskorte, N.; Mur, M.; and Bandettini, P. A. 2008. Representational Similarity Analysis – Connecting the Branches of Systems Neuroscience. *Frontiers in Systems Neuroscience*.
- Krizhevsky, A.; Sutskever, I.; and Hinton, G. E. 2012. ImageNet classification with deep convolutional neural networks. In *NeurIPS*.
- Kullback, S.; and Leibler, R. A. 1951. On information and sufficiency. *Annals of Mathematical Statistics*, 22(1): 79–86.
- Lafon, M.; Ramzi, E.; Rambour, C.; Audebert, N.; and Thome, N. 2024. Gallop: Learning global and local prompts for vision-language models. In *ECCV*.
- Li, S.; Liu, F.; Hao, Z.; Wang, X.; Li, L.; Liu, X.; Chen, P.; and Ma, W. 2025. Logits DeConfusion with CLIP for Few-Shot Learning. In *CVPR*, 25411–25421.
- Maji, S.; Rahtu, E.; Kannala, J.; Blaschko, M. B.; and Vedaldi, A. 2013. Fine-Grained Visual Classification of Aircraft. *CoRR*, abs/1306.5151.
- Mémoli, F. 2011. Gromov–Wasserstein distances and the metric approach to object matching. *Foundations of computational mathematics*.
- Nilsback, M.; and Zisserman, A. 2008. Automated Flower Classification over a Large Number of Classes. In *Sixth Indian Conference on Computer Vision, Graphics & Image Processing, ICVGIP 2008, Bhubaneswar, India, 16-19 December 2008*, 722–729.
- Pal, A.; van Spengler, M.; di Melendugno, G. M. D.; Flaborea, A.; Galasso, F.; and Mettes, P. 2025. Compositional Entailment Learning for Hyperbolic Vision-Language Models. In *ICLR*.
- Parkhi, O. M.; Vedaldi, A.; Zisserman, A.; and Jawahar, C. V. 2012. Cats and dogs. In *CVPR*.
- Radford, A.; Kim, J. W.; Hallacy, C.; Ramesh, A.; Goh, G.; Agarwal, S.; Sastry, G.; Askell, A.; Mishkin, P.; Clark, J.; Krueger, G.; and Sutskever, I. 2021. Learning Transferable Visual Models From Natural Language Supervision. In *ICML*.
- Recht, B.; Roelofs, R.; Schmidt, L.; and Shankar, V. 2019. Do ImageNet Classifiers Generalize to ImageNet? In *ICML*.
- Soomro, K.; Zamir, A. R.; and Shah, M. 2012. UCF101: A Dataset of 101 Human Actions Classes From Videos in The Wild. *CoRR*, abs/1212.0402.
- Sun, Q.; Fang, Y.; Wu, L. Y.; Wang, X.; and Cao, Y. 2023. EVA-CLIP: Improved Training Techniques for CLIP at Scale. *ArXiv*.
- Tang, Y.; Lin, Z.; Wang, Q.; Zhu, P.; and Hu, Q. 2024. Amu-tuning: Effective logit bias for clip-based few-shot learning. In *CVPR*.



Tschannen, M.; Gritsenko, A.; Wang, X.; Naeem, M. F.; Alabdulmohsin, I.; Parthasarathy, N.; Evans, T.; Beyer, L.; Xia, Y.; Mustafa, B.; et al. 2025. SigLIP 2: Multilingual Vision-Language Encoders with Improved Semantic Understanding, Localization, and Dense Features. *arXiv preprint arXiv:2502.14786*.

Wang, H.; Ge, S.; Lipton, Z. C.; and Xing, E. P. 2019. Learning Robust Global Representations by Penalizing Local Predictive Power. In *NeurIPS*.

Wu, S.; Zhang, J.; Zeng, P.; Gao, L.; Song, J.; and Shen, H. T. 2025. Skip tuning: Pre-trained vision-language models are effective and efficient adapters themselves. In *CVPR*.

Xiao, J.; Hays, J.; Ehinger, K. A.; Oliva, A.; and Torralba, A. 2010. SUN database: Large-scale scene recognition from abbey to zoo. In *CVPR*.

Xie, J.; Zhang, Y.; Peng, J.; Huang, Z.; and Cao, L. 2024. TextRefiner: Internal Visual Feature as Efficient Refiner for Vision-Language Models Prompt Tuning. *arXiv preprint arXiv:2412.08176*.

Xu, H.; Xie, S.; Tan, X. E.; Huang, P.; Howes, R.; Sharma, V.; Li, S.; Ghosh, G.; Zettlemoyer, L.; and Feichtenhofer, C. 2024. Demystifying CLIP Data. In *The Twelfth International Conference on Learning Representations, ICLR 2024, Vienna, Austria, May 7-11, 2024*.

Yang, L.; Zhang, R.-Y.; Wang, Y.; and Xie, X. 2024. Mma: Multi-modal adapter for vision-language models. In *Proceedings of the IEEE/CVF Conference on Computer Vision and Pattern Recognition*.

Yao, H.; Zhang, R.; and Xu, C. 2024. TCP: Textual-based Class-aware Prompt tuning for Visual-Language Model. In *CVPR*.

Yu, T.; Lu, Z.; Jin, X.; Chen, Z.; and Wang, X. 2023. Task Residual for Tuning Vision-Language Models. In *CVPR*.

Zeiler, M. 2014. Visualizing and Understanding Convolutional Networks. In *ECCV*.

Zhai, X.; Mustafa, B.; Kolesnikov, A.; and Beyer, L. 2023. Sigmoid Loss for Language Image Pre-Training. In *ICCV*.

Zhang, J.; Wu, S.; Gao, L.; Shen, H. T.; and Song, J. 2024. Dept: Decoupled prompt tuning. In *Proceedings of the IEEE/CVF Conference on Computer Vision and Pattern Recognition*.

Zhang, R.; Zhang, W.; Fang, R.; Gao, P.; Li, K.; Dai, J.; Qiao, Y.; and Li, H. 2022. Tip-Adapter: Training-Free Adaption of CLIP for Few-Shot Classification. In *ECCV*.

Zhou, K.; Yang, J.; Loy, C. C.; and Liu, Z. 2022a. Conditional Prompt Learning for Vision-Language Models. In *CVPR*.

Zhou, K.; Yang, J.; Loy, C. C.; and Liu, Z. 2022b. Learning to Prompt for Vision-Language Models. *International Journal of Computer Vision*, 130(9): 2337–2348.

Zhu, B.; Niu, Y.; Han, Y.; Wu, Y.; and Zhang, H. 2023. Prompt-aligned gradient for prompt tuning. In *ICCV*.

Zhu, Y.; Ji, Y.; Zhao, Z.; Wu, G.; and Wang, L. 2024. AWT: Transferring Vision-Language Models via Augmentation, Weighting, and Transportation. *arXiv preprint arXiv:2407.04603*.

# Preserve and Sculpt: Manifold-Aligned Fine-tuning of Vision-Language Models for Few-Shot Learning

## Appendix

### A. Detailed Proof for the Upper Bound on Gromov-Wasserstein Distance

**Theorem 2** *The alignment of Gram matrices under the  $L_p$ -norm serves as a tractable upper bound for the  $p$ -th order Gromov-Wasserstein distance ( $GW_p$ ), when the underlying metric is the cosine distance.*

**Proof 1** *The objective is to formally demonstrate that the Manifold Alignment Regularization (MAR) strategy, which aligns Gram matrices, minimizes a computationally tractable upper bound of the  $p$ -th order Gromov-Wasserstein (GW) distance between the feature manifolds of the original pre-trained model and the fine-tuned model.*

**1. Definition of Metric Spaces.** We consider two discrete metric probability spaces,  $(\mathcal{X}, d_{\mathcal{X}}, \mu)$  and  $(\mathcal{Y}, d_{\mathcal{Y}}, \nu)$ .

- **Space  $\mathcal{X}$ :** Represents the feature space of the original, frozen model. For a mini-batch of  $N$  samples, we extract a set of normalized features  $Z = \{z_1, z_2, \dots, z_N\}$ , where  $z_i \in \mathbb{R}^d$ .
- **Space  $\mathcal{Y}$ :** Represents the feature space of the fine-tuned model. For the same mini-batch, the corresponding set of normalized features is  $Z' = \{z'_1, z'_2, \dots, z'_N\}$ , where  $z'_i \in \mathbb{R}^d$ .
- **Metric  $d$ :** We employ the **Cosine Distance** as the metric. For a pair of normalized vectors  $a$  and  $b$ , the distance is  $d(a, b) = 1 - \langle a, b \rangle$ . The intra-space distance matrices,  $D_Z$  and  $D_{Z'}$ , are thus:

$$(D_Z)_{ij} = d(z_i, z_j) = 1 - \langle z_i, z_j \rangle \quad (13)$$

$$(D_{Z'})_{ij} = d(z'_i, z'_j) = 1 - \langle z'_i, z'_j \rangle \quad (14)$$

- **Probability Distributions  $\mu, \nu$ :** For a discrete batch of  $N$  samples, we assume a uniform probability distribution, i.e.,  $\mu = \nu = \frac{1}{N} \sum_{i=1}^N \delta_i$ , where  $\delta_i$  is the Dirac measure.

**2. Gromov-Wasserstein Distance and the Concept of Coupling.** The discrete  $p$ -th order GW distance is formulated as:

$$GW_p(\mu, \nu) = \left( \min_{\pi \in \Pi(\mu, \nu)} \sum_{i,j=1}^N \sum_{k,l=1}^N |(D_Z)_{ij} - (D_{Z'})_{kl}|^p \pi_{ik} \pi_{jl} \right)^{1/p} \quad (15)$$

Here,  $\pi \in \Pi(\mu, \nu)$  is a **coupling**, which is a joint probability distribution over the product space  $\mathcal{X} \times \mathcal{Y}$ . Intuitively, a coupling can be understood as a probabilistic transportation plan that describes how to map or associate the points from space  $\mathcal{X}$  (with distribution  $\mu$ ) to the points in space  $\mathcal{Y}$  (with distribution  $\nu$ ). The GW distance seeks the optimal coupling  $\pi^*$  that minimizes the expected difference between pairwise

distances in the two spaces. Finding this optimal plan involves solving a quadratic assignment problem, which is computationally intractable (NP-hard) for non-trivial cases.

**3. Simplification via a Fixed Coupling.** To derive a computationally feasible upper bound, we forgo the optimization over all possible couplings and instead select a single, fixed coupling. As outlined in the paper, we adopt a natural coupling,  $\pi_{\text{nat}}$ , which assumes a one-to-one correspondence between the features of the same sample before and after fine-tuning. This coupling is formally defined as:

$$\pi_{\text{nat},ik} = \begin{cases} 1/N & \text{if } i = k \\ 0 & \text{if } i \neq k \end{cases} \quad (16)$$

By definition, the GW distance is the minimum over all couplings. Therefore, using our specific  $\pi_{\text{nat}}$  provides an upper bound on the true GW distance.

**4. Derivation of the Upper Bound.** We substitute our fixed coupling  $\pi_{\text{nat}}$  into the  $p$ -th power of the GW distance formula:

$$GW_p(\mu, \nu)^p \leq \sum_{i,j=1}^N \sum_{k,l=1}^N |(D_Z)_{ij} - (D_{Z'})_{kl}|^p \cdot \pi_{\text{nat},ik} \pi_{\text{nat},jl} \quad (17)$$

Due to the structure of  $\pi_{\text{nat}}$ , the term  $\pi_{\text{nat},ik} \pi_{\text{nat},jl}$  is non-zero only when  $i = k$  and  $j = l$ , where it evaluates to  $(1/N)(1/N) = 1/N^2$ . This simplifies the quadruple summation into a double summation:

$$GW_p(\mu, \nu)^p \leq \frac{1}{N^2} \sum_{i=1}^N \sum_{j=1}^N |(D_Z)_{ij} - (D_{Z'})_{ij}|^p \quad (18)$$

**5. Connection to Manifold Alignment Regularization (MAR).** Let  $S$  and  $S'$  denote the Gram matrices (cosine similarity matrices). The absolute difference in distances can be expressed in terms of the Gram matrices:

$$\begin{aligned} |(D_Z)_{ij} - (D_{Z'})_{ij}| &= |(1 - \langle z_i, z_j \rangle) - (1 - \langle z'_i, z'_j \rangle)| \\ &= |S'_{ij} - S_{ij}| \end{aligned} \quad (19)$$

Substituting this back into our inequality, we arrive at the final upper bound:

$$GW_p(\mu, \nu)^p \leq \frac{1}{N^2} \sum_{i=1}^N \sum_{j=1}^N |S'_{ij} - S_{ij}|^p \quad (20)$$

This expression shows that the  $p$ -th power of the GW distance is upper-bounded by the scaled  $L_p$ -norm of the difference between the Gram matrices of the two feature spaces.

Table 6: Performance comparison on CLIP benchmark on ViT-B/16.

Method	Setting	ImageNet	Caltech101	OxfordPets	StanfordCars	Flowers102	Food101	FGVCAircraft	SUN397	DTD	EuroSAT	UCF101	Average
CLIP (Radford et al. 2021)	1-shot	66.73	93.35	88.25	65.48	67.44	83.65	23.67	62.59	44.27	42.01	65.13	63.87
CoOp (Zhou et al. 2022b)		66.33	92.60	90.37	67.43	77.53	84.33	21.37	66.77	50.23	54.93	71.23	67.56
Tip-adapter-F (Zhang et al. 2022)		69.83	93.83	90.84	67.88	<b>87.37</b>	<b>86.17</b>	30.39	67.42	53.72	64.35	73.70	71.41
PLOT++ (Chen et al. 2023)		66.45	94.34	91.89	68.81	80.48	86.16	28.60	66.77	54.57	65.41	74.31	70.71
TaskRes (Yu et al. 2023)		69.57	93.53	90.17	68.83	85.77	84.57	31.30	68.13	53.80	65.43	71.70	71.16
MaPLe (Khattak et al. 2023a)		68.73	93.67	91.53	68.07	78.80	84.40	27.97	68.40	50.97	41.90	72.60	67.91
PromptSRC (Khattak et al. 2023b)		68.13	93.67	92.00	69.40	85.93	84.87	27.67	69.67	56.23	73.13	74.80	72.32
AMU-Tuning (Tang et al. 2024)		67.37	94.51	91.01	65.65	80.29	85.15	27.20	65.11	51.77	70.76	71.89	70.07
TCP (Yao, Zhang, and Xu 2024)		67.03	93.53	91.43	66.17	86.87	84.67	28.87	69.00	54.80	62.53	73.37	70.75
DePT (Zhang et al. 2024)		64.23	93.70	90.43	67.63	82.77	84.70	30.03	68.03	54.07	52.30	74.03	69.27
GallLop (Lafon et al. 2024)		69.79	94.11	91.59	<b>71.47</b>	86.12	84.81	<b>32.52</b>	68.82	57.15	63.58	73.11	72.10
TextRefiner (Xie et al. 2024)		69.00	92.13	88.17	65.07	70.10	85.40	25.63	67.97	44.83	53.93	69.93	66.56
MMRL (Guo and Gu 2025)		69.00	94.17	90.87	68.70	85.97	84.87	28.53	68.90	56.37	76.00	75.97	72.67
SkipT (Wu et al. 2025)		69.20	93.87	91.60	69.63	83.63	85.67	29.93	69.10	54.50	72.23	75.30	72.24
LDC (Li et al. 2025)		69.54	93.79	91.25	68.24	83.64	85.88	27.57	<b>67.99</b>	<b>58.22</b>	<b>78.49</b>	73.20	72.53
TAC (Hao et al. 2025)		69.80	<b>94.60</b>	<b>92.10</b>	71.33	85.27	85.70	31.17	<b>71.17</b>	56.87	70.47	76.47	73.18
MPS-Tuning (Ours)		<b>70.37</b>	<b>94.47</b>	<b>91.17</b>	70.17	<b>86.50</b>	<b>86.10</b>	29.97	<b>70.40</b>	<b>56.47</b>	<b>76.10</b>	<b>77.40</b>	<b>73.55</b>
CLIP (Radford et al. 2021)	2-shot	66.73	93.35	88.25	65.48	67.44	83.65	23.67	62.59	44.27	42.01	65.13	63.87
CoOp (Zhou et al. 2022b)		67.07	93.07	89.80	70.50	87.33	84.40	26.20	66.53	53.60	65.17	73.43	70.65
Tip-adapter-F (Zhang et al. 2022)		70.04	94.20	91.47	70.91	89.65	86.39	33.51	68.64	55.91	73.17	76.10	73.64
PLOT++ (Chen et al. 2023)		68.28	94.69	92.29	73.17	89.81	86.33	31.14	68.06	56.72	76.80	76.76	74.00
TaskRes (Yu et al. 2023)		70.20	94.23	90.67	72.07	89.70	85.60	32.67	70.43	55.67	70.23	75.20	73.33
MaPLe (Khattak et al. 2023a)		69.47	94.20	92.63	69.80	84.47	85.03	30.93	70.53	55.63	72.30	74.30	72.66
PromptSRC (Khattak et al. 2023b)		69.77	94.53	92.50	73.40	91.17	85.70	31.70	71.60	59.97	79.37	78.50	75.29
AMU-Tuning (Tang et al. 2024)		69.62	94.86	90.41	68.52	83.31	85.51	31.15	67.67	54.04	72.55	74.85	72.04
TCP (Yao, Zhang, and Xu 2024)		68.30	94.13	90.57	71.00	90.87	85.17	32.23	71.03	58.43	70.63	77.70	73.64
DePT (Zhang et al. 2024)		65.97	94.27	90.90	71.77	88.80	85.30	32.43	70.37	59.83	68.57	77.60	73.25
GallLop (Lafon et al. 2024)		70.57	95.25	<b>93.09</b>	75.03	<b>91.81</b>	85.42	<b>36.74</b>	71.17	61.90	67.83	77.81	75.15
TextRefiner (Xie et al. 2024)		70.10	93.37	90.10	65.17	73.37	85.70	26.63	69.07	48.70	53.40	69.77	67.76
MMRL (Guo and Gu 2025)		70.30	94.83	91.57	72.93	91.20	85.53	34.23	71.53	61.37	<b>82.87</b>	78.50	75.90
SkipT (Wu et al. 2025)		70.23	95.10	92.43	73.17	90.33	85.90	33.53	70.60	58.83	78.50	78.37	75.18
LDC (Li et al. 2025)		69.86	94.32	91.17	70.75	88.71	86.07	28.98	69.61	<b>62.17</b>	81.73	75.95	74.48
TAC (Hao et al. 2025)		70.73	95.27	92.63	74.80	91.10	86.30	36.37	<b>72.97</b>	60.93	80.97	79.30	76.49
MPS-Tuning (Ours)		<b>71.43</b>	<b>95.50</b>	92.40	<b>75.37</b>	91.57	<b>86.70</b>	33.77	72.37	61.47	81.63	<b>81.03</b>	<b>76.66</b>
CLIP (Radford et al. 2021)	4-shot	66.73	93.35	88.25	65.48	67.44	83.65	23.67	62.59	44.27	42.01	65.13	63.87
CoOp (Zhou et al. 2022b)		68.73	94.40	92.57	74.47	92.17	84.47	30.83	69.97	58.70	70.80	77.10	74.02
Tip-adapter-F (Zhang et al. 2022)		70.70	95.01	92.04	74.57	92.61	86.67	36.45	70.77	61.70	79.22	79.51	76.30
PLOT++ (Chen et al. 2023)		70.40	95.13	92.55	76.25	92.93	86.46	35.29	71.73	62.43	83.21	79.76	76.92
TaskRes (Yu et al. 2023)		70.93	95.00	91.93	75.97	91.73	86.03	33.40	72.70	60.17	74.17	76.20	75.29
MaPLe (Khattak et al. 2023a)		70.77	95.30	93.27	71.97	90.47	85.67	32.63	72.73	61.17	76.57	77.93	75.32
PromptSRC (Khattak et al. 2023b)		71.07	95.27	93.43	77.13	93.87	86.17	37.47	74.00	65.53	86.30	81.57	78.35
AMU-Tuning (Tang et al. 2024)		71.69	96.21	92.31	71.52	86.28	85.77	34.48	70.24	59.32	78.63	76.67	74.83
TCP (Yao, Zhang, and Xu 2024)		69.97	95.17	92.00	76.43	93.83	85.50	36.37	73.40	64.07	73.63	80.77	76.47
DePT (Zhang et al. 2024)		68.57	95.10	92.83	76.13	93.87	85.70	34.57	73.07	64.13	78.87	81.03	76.72
GallLop (Lafon et al. 2024)		71.67	95.60	93.22	79.69	95.58	86.08	<b>42.65</b>	73.42	66.88	74.05	81.23	78.19
TextRefiner (Xie et al. 2024)		70.70	93.13	92.57	67.90	76.17	87.03	29.43	70.80	51.37	56.00	71.87	69.72
MMRL (Guo and Gu 2025)		71.40	96.03	92.57	78.17	94.60	85.77	40.47	73.93	67.87	87.67	82.67	79.20
SkipT (Wu et al. 2025)		71.40	95.60	93.33	77.60	94.27	86.00	39.90	73.07	65.70	83.40	82.53	78.44
LDC (Li et al. 2025)		71.04	95.25	91.80	75.13	93.95	86.71	31.92	72.92	66.43	86.37	79.75	77.39
TAC (Hao et al. 2025)		71.73	95.60	<b>93.67</b>	78.63	94.50	86.80	41.93	<b>74.70</b>	66.67	<b>88.70</b>	82.93	79.62
MPS-Tuning (Ours)		<b>72.57</b>	<b>96.80</b>	<b>93.67</b>	<b>81.17</b>	<b>96.00</b>	<b>87.17</b>	41.97	<b>74.53</b>	<b>68.50</b>	<b>88.50</b>	<b>84.30</b>	<b>80.47</b>
CLIP (Radford et al. 2021)	8-shot	66.73	93.35	88.25	65.48	67.44	83.65	23.67	62.59	44.27	42.01	65.13	63.87
CoOp (Zhou et al. 2022b)		70.63	94.37	91.27	79.30	94.97	82.67	39.00	71.53	64.77	78.07	80.20	76.98
Tip-adapter-F (Zhang et al. 2022)		72.01	95.17	91.88	77.91	94.88	86.80	41.94	73.93	67.91	84.35	82.37	79.01
PLOT++ (Chen et al. 2023)		71.31	95.51	93.02	81.26	95.44	86.58	41.42	73.93	66.49	88.37	82.80	79.65
TaskRes (Yu et al. 2023)		72.20	95.30	92.00	79.60	96.70	86.40	40.27	74.57	66.60	77.47	81.67	78.43
MaPLe (Khattak et al. 2023a)		71.63	95.40	93.07	74.63	94.27	86.47	36.97	74.00	65.57	84.60	81.03	77.97
PromptSRC (Khattak et al. 2023b)		72.33	95.67	93.50	80.97	96.27	86.90	43.27	75.73	69.87	88.80	84.30	80.69
AMU-Tuning (Tang et al. 2024)		73.56	96.74	93.34	74.62	89.38	86.04	38.86	71.32	61.39	80.78	79.59	76.87
TCP (Yao, Zhang, and Xu 2024)		71.60	95.43	92.30	80.27	96.20	86.53	40.93	75.07	68.80	77.57	83.23	78.90
DePT (Zhang et al. 2024)		71.37	95.70	93.47	80.63	96.27	86.60	41.00	75.30	69.40	82.83	83.57	79.65
GallLop (Lafon et al. 2024)		72.86	96.19	93.73	84.42	97.90	86.79	48.48	75.51	71.89	84.04	84.40	81.48
TextRefiner (Xie et al. 2024)		70.77	95.17	92.70	69.87	84.07	86.97	31.00	72.17	55.23	59.57	75.37	72.08
MMRL (Guo and Gu 2025)		72.33	96.27	93.03	82.57	96.60	86.33	48.07	76.00	71.60	88.73	84.67	81.47
SkipT (Wu et al. 2025)		72.40	95.90	93.40	82.33	96.60	86.73	46.50	74.77	69.77	86.57	85.60	80.96
LDC (Li et al. 2025)		72.48	95.86	92.48	79.69	95.98	86.94	37.98	75.56	71.51	90.80	80.91	80.02
TAC (Hao et al. 2025)		72.73	96.27	<b>94.20</b>	82.43	96.53	87.20	48.63	76.17	70.73	89.63	85.83	81.85
MPS-Tuning (Ours)		<b>74.07</b>	<b>96.83</b>	<b>93.77</b>	<b>87.20</b>	<b>98.03</b>	<b>87.63</b>	<b>55.60</b>	<b>76.70</b>	<b>73.30</b>	<b>91.13</b>	<b>87.03</b>	<b>83.75</b>
CLIP (Radford et al. 2021)	16-shot	66.73	93.35	88.25	65.48	67.44	83.65	23.67	62.59	44.27	42.01	65.13	63.87
CoOp (Zhou et al. 2022b)		71.87	95.57	91.87	83.07	97.07	84.20	43.40	74.67	69.87	84.93	82.23	79.89
Tip-adapter-F (Zhang et al. 2022)		73.71	96.11	93.02	83.68	96.26	87.34	45.03	76.30	72.46	88.47	85.12	81.59
PLOT++ (Chen et al. 2023)		72.60	96.04	93.59	84.55	97.56	87.11	46.74	76.03	71.43	92.00	85.34	82.09
TaskRes (Yu et al. 2023)		73.03	95.80	92.40	83.47	97.93	86.90	44.90	76.07	71.57	82.70	83.97	80.79
MaPLe (Khattak et al. 2023a)		72.57	95.67	93.30	78.00	95.80	87.37	40.63	75.47	70.50	89.03	82.70	80.09
PromptSRC (Khattak et al. 2023b)		73.17	96.07	93.67	83.83	97.60	87.50	50.83	77.23	72.73	92.43	86.47	82.87
AMU-Tuning (Tang et al. 2024)		74.93	97.04	93.46	78.10	90.95	86.40	43.12	72.78	64.66	82.14	80.54	78.56
TCP (Yao, Zhang, and Xu 2024)		72.40	95.83	92.77	84.00	97.43	87.23	46.13	76.80	72.70	85.00	85.40	81.43
DePT (Zhang et al. 2024)		73.35	96.27	94.13	85.03	97.83	87.30	47.00	77.30	74.03	91.43	85.57	82.66
GallLop (Lafon et al. 2024)													

$L_1$ -norm ( $p = 1$ ). This provides a strong theoretical justification for how aligning Gram matrices effectively preserves the geometric structure of the feature manifold during fine-tuning.

## B. Hyperparameter Settings

This section provides a detailed overview of the hyperparameter settings used in our experiments for MPS-Tuning. The primary hyperparameter values, which serve as the default for most datasets, are presented in Table 11. All experiments were conducted using the CLIP ViT-B/16 as the base model and were averaged over three different random seeds to ensure the reliability of our results.

While most parameters were kept consistent to ensure a fair evaluation, certain key hyperparameters were adjusted for specific datasets to optimize performance. Specifically, the weight for the Manifold Alignment Regularization loss ( $\lambda_1$ ) was increased to 2.0 for datasets with natural images, namely ImageNet, OxfordPets, Food101, and SUN397, to enforce stronger preservation of the rich pre-trained manifold. For all other datasets, the default value of 0.5 was used. Similarly, the batch size was set to 64 for the large-scale ImageNet dataset to ensure stable gradient estimation, while a batch size of 32 was used for all other datasets.

Furthermore, we employed a dynamic temperature scheduling for the HMS loss ( $\tau'$ ) using a cosine annealing strategy over the training epochs. For datasets including OxfordPets, Food101, DescribableTextures, EuroSAT, and UCF101, the temperature was annealed from an initial value of 0.5 down to 0.07. For the remaining datasets, a more conservative schedule from 0.1 to 0.05 was applied.

To mitigate the risk of overfitting caused by excessive category-specific supervision on intermediate layers, we incorporate a simple layer-wise decay scheme in HMS. Concretely, the final layer is assigned a weight of 1, and the weight of each preceding layer is defined recursively as half that of its subsequent layer:

$$w_L = 1, \quad w_l = \frac{1}{2} w_{l+1} \quad \text{for } l = L-1, L-2, \dots, 1, \quad (21)$$

where  $L$  denotes the total number of layers.

Regarding data augmentation, we followed the standard protocol used in CoOp. This includes ‘RandomResized-Crop’ with a scale range of (0.3, 1.0) and random horizontal flipping. No other complex augmentations were used.

## C. Trainable Modules

Benefiting from the powerful regularization capacity of MAR, direct fine-tuning of pre-trained models becomes feasible in few-shot scenarios. Specifically, a hierarchical fine-tuning strategy is employed for the visual encoder. The modules in the ViT/B-16 backbone are grouped based on semantic hierarchy (Gandelsman, Efros, and Steinhardt 2024), with every four layers forming a group. The first group remains frozen during training to retain general representation learning. In the second group, each Transformer block is

paired with a zero-initialized linear layer operating in parallel. Inputs are processed by both branches, and their outputs are summed to allow lightweight adjustments in intermediate representations. The third group is fully fine-tuned to facilitate adaptation to downstream tasks.

## D. Datasets

In the main text, our method was assessed on the widely adopted CLIP Benchmark, in alignment with previous work (Zhou et al. 2022b; Zhang et al. 2022; Yu et al. 2023). The benchmark comprises 11 diverse datasets, including ImageNet (Deng et al. 2009), Caltech101 (Fei-Fei, Fergus, and Perona 2007), Oxford Pets (Parkhi et al. 2012), Stanford Cars (Krause et al. 2013), Flowers102 (Nilsback and Zisserman 2008), Food101 (Bossard, Guillaumin, and Gool 2014), FGVC Aircraft (Maji et al. 2013), SUN397 (Xiao et al. 2010), DTD (Cimpoi et al. 2014), EuroSAT (Helber et al. 2019), and UCF101 (Soomro, Zamir, and Shah 2012). These datasets span a broad range of image classification scenarios, encompassing general object recognition, fine-grained object recognition, scene recognition, texture recognition, and satellite imagery analysis. To ensure consistency with previous work (Zhou et al. 2022b; Zhang et al. 2022; Yu et al. 2023), the ‘BACKGROUND Google’ and ‘Faces easy’ classes were excluded from the Caltech101 dataset. Additionally, robustness under domain shift was analyzed using two ImageNet variants: ImageNet-V2 (Recht et al. 2019), containing 200 overlapping classes, and ImageNet-Sketch (Wang et al. 2019), encompassing 1,000 classes identical to ImageNet. Consistent with earlier works, ImageNet was used as the source dataset, while the two variants served as target datasets. An overview of these datasets is presented in Tab. 7.

## E. Numerical Results

Comparative evaluations were conducted across 11 benchmark datasets against state-of-the-art methods, including CoOp (Zhou et al. 2022b), Tip-Adapter-F (Zhang et al. 2022), PLOT++ (Chen et al. 2023), MaPle (Khattak et al. 2023a), PromptSRC (Khattak et al. 2023b), AMU-Tuning (Tang et al. 2024), TCP (Yao, Zhang, and Xu 2024), DePT (Zhang et al. 2024), GalLop (Lafon et al. 2024), TextRefiner (Xie et al. 2024), MMRL (Guo and Gu 2025), SkipT (Wu et al. 2025), LDC (Li et al. 2025), and TAC (Hao et al. 2025). Our approach achieved the highest average performance under all few-shot settings (1, 2, 4, 8, and 16 shots), with its advantage becoming increasingly pronounced as more samples were introduced, underscoring its robust learning capability.

## F. Sensitivity Study

We conducted sensitivity analyses for the weights of MAR ( $\lambda_1$ ), HMS ( $\lambda_2$ ), and the logits from the fine-tuning branch ( $\alpha$ ), with the corresponding results shown in Tables Tab. 8, Tab. 9, and Tab. 10, respectively. Regarding  $\lambda_1$ , we found that setting it to 0.5 or 1 yields the best performance when a fixed value is applied across all datasets. To further improve performance, we divided the datasets into two groups

Table 7: Summary of 11 datasets for few-shot learning and 2 target datasets of domain generalization. The 7 selected templates (Zhang et al. 2022) for ImageNet series datasets are “itap of a [class].”, “a bad photo of the [class].”, “a origami [class].”, “a photo of the large [class].”, “a [class] in a video game.”, “art of the [class].” and “a photo of the small [class].”

Name	Number of Classes	Size (Train / Val / Test)	Description	Template
ImageNet (Deng et al. 2009)	1000	1.28M / - / 50000	Recognition of generic objects	Ensemble of 7 selected templates
ImageNet-V2 (Recht et al. 2019)	1000	- / - / 10000	New test data for ImageNet	
ImageNet-Sketch (Wang et al. 2019)	1000	- / - / 50889	Sketch-style images of ImageNet classes	
Caltech101 (Fei-Fei, Fergus, and Perona 2007)	100	4128 / 1649 / 2465	Recognition of generic objects	“a photo of a [class].”
OxfordPets (Parkhi et al. 2012)	37	2944 / 736 / 3669	Fine-grained classification of pets	“a photo of a [class], a type of pet.”
StanfordCars (Krause et al. 2013)	196	6509 / 1635 / 8041	Fine-grained classification of cars	“a photo of a [class].”
Flowers102 (Nilsback and Zisserman 2008)	102	4093 / 1633 / 2463	Fine-grained classification of flowers	“a photo of a [class], a type of flower.”
Food101 (Bossard, Guillaumin, and Gool 2014)	101	50500 / 20200 / 30300	Fine-grained classification of foods	“a photo of a [class], a type of food.”
FGVCAircraft (Maji et al. 2013)	100	3334 / 3333 / 3333	Fine-grained classification of aircrafts	“a photo of a [class], a type of aircraft.”
SUN397 (Xiao et al. 2010)	397	15880 / 3970 / 19850	Scene classification	“a photo of a [class].”
DTD (Cimpoi et al. 2014)	47	2820 / 1128 / 1692	Texture classification	“[class] texture.”
EuroSAT (Helber et al. 2019)	10	13500 / 5400 / 8100	Land use & cover classification with satellite images	“a centered satellite photo of [class].”
UCF101 (Soomro, Zamir, and Shah 2012)	101	7639 / 1898 / 3783	Action recognition	“a photo of a person doing [class].”

Table 8: Sensitivity Study on MAR weight  $\lambda_1$

$\lambda_1$	ImageNet	Caltech101	OxfordPets	StanfordCars	Flowers102	Food101	FGVCAircraft	SUN397	DTD	EuroSAT	UCF101	Average
0.01	74.80	97.33	93.67	90.70	99.23	86.27	68.43	77.87	76.53	94.20	89.17	86.20
0.1	74.97	<b>97.43</b>	94.33	90.97	99.33	87.13	68.60	78.07	76.97	94.40	89.67	86.53
0.2	74.97	<b>97.43</b>	94.37	90.90	99.33	87.20	68.83	78.07	77.10	<b>94.43</b>	89.80	86.58
0.5	75.23	<b>97.43</b>	94.53	<b>91.13</b>	99.37	87.70	<b>69.03</b>	78.37	77.20	94.37	<b>89.87</b>	86.74
1	75.43	<b>97.43</b>	94.70	90.97	<b>99.40</b>	88.00	68.83	78.43	<b>77.30</b>	93.37	89.63	<b>86.76</b>
2	<b>75.60</b>	97.23	<b>94.77</b>	90.77	99.20	<b>88.13</b>	68.23	<b>78.47</b>	76.93	92.10	88.90	86.39
5	75.47	96.93	94.37	90.03	98.83	88.03	66.50	78.13	76.33	91.30	88.20	85.83
10	75.13	96.73	94.13	88.30	98.53	88.00	64.43	77.90	76.07	91.27	87.47	85.27

Table 9: Sensitivity Study on HMS weight  $\lambda_2$

	ImageNet	Caltech101	OxfordPets	StanfordCars	Flowers102	Food101	FGVCAircraft	SUN397	DTD	EuroSAT	UCF101	Average
0.01	75.37	97.13	94.37	91.03	99.27	88.03	68.93	78.10	<b>77.20</b>	93.73	89.17	86.58
0.1	75.60	97.37	94.77	<b>91.13</b>	<b>99.37</b>	<b>88.13</b>	<b>69.03</b>	78.47	<b>77.20</b>	94.37	<b>89.87</b>	<b>86.85</b>
0.2	<b>75.63</b>	<b>97.47</b>	<b>94.87</b>	91.07	99.20	88.07	66.73	<b>78.50</b>	76.93	94.33	89.77	86.60
0.3	75.60	97.27	94.73	91.00	99.13	87.87	66.93	78.30	76.97	<b>94.40</b>	89.63	86.53
0.5	75.50	95.27	94.57	90.67	99.10	87.07	67.63	77.77	76.80	94.27	89.33	86.18
0.8	74.90	93.70	94.13	88.73	98.80	86.57	63.37	66.33	75.77	93.63	88.23	84.02
1	74.90	96.37	93.93	88.17	98.27	86.33	50.83	67.87	75.83	94.17	88.07	83.16
2	69.07	91.93	93.27	80.03	86.60	84.77	24.43	64.53	43.20	87.30	83.83	73.82

Table 10: Sensitivity Study on logits weight  $\alpha$

	ImageNet	Caltech101	OxfordPets	StanfordCars	Flowers102	Food101	FGVCAircraft	SUN397	DTD	EuroSAT	UCF101	Average
0.1	74.07	96.97	94.43	88.30	95.50	87.90	58.33	75.60	71.47	91.70	87.60	83.81
0.2	75.43	97.27	<b>94.77</b>	90.83	99.23	88.10	68.00	78.07	76.83	93.87	89.40	86.53
0.3	75.60	97.37	<b>94.77</b>	<b>91.13</b>	<b>99.37</b>	<b>88.13</b>	69.03	78.47	77.20	<b>94.37</b>	89.87	<b>86.85</b>
0.4	<b>75.67</b>	97.40	94.63	<b>91.13</b>	<b>99.37</b>	88.07	68.87	78.57	<b>77.30</b>	94.20	<b>89.90</b>	86.83
0.5	75.57	97.37	94.57	<b>91.13</b>	99.33	87.87	68.97	<b>78.67</b>	77.17	94.17	89.80	86.78
0.6	75.50	97.33	94.30	90.97	99.27	87.63	68.87	78.60	77.17	94.00	89.57	86.65
0.7	75.33	97.40	93.63	90.70	99.13	87.07	<b>69.17</b>	78.50	76.60	94.13	89.27	86.45
0.8	75.00	<b>97.47</b>	92.97	89.80	98.97	86.33	67.90	78.27	76.40	93.20	88.93	85.93
0.9	74.57	97.20	91.37	89.33	99.00	84.93	67.73	77.83	76.63	93.00	88.57	85.47
1.0	74.00	97.07	89.00	88.33	98.80	83.03	67.10	77.20	75.87	93.37	87.87	84.69

and set  $\lambda_1$  to 0.5 and 2 for each group (see Hyperparameter Settings), respectively. As for  $\lambda_2$ , we fixed it at 0.1 across

all datasets, and similarly,  $\alpha$  was set to 0.3 for all datasets. Notably, the model’s performance exhibited minimal varia-



Table 11: Default hyperparameter settings used for training MPS-Tuning.

Hyperparameter	Value
Optimizer	SGD
Batch Size	32
Total Epochs	50
Peak Learning Rate	0.002
LR Scheduler	Cosine Decay
Logits Weight $\alpha$	0.3
MAR Loss Weight $\lambda_1$	0.5
HMS Loss Weight $\lambda_2$	0.1
HMS Depth	2

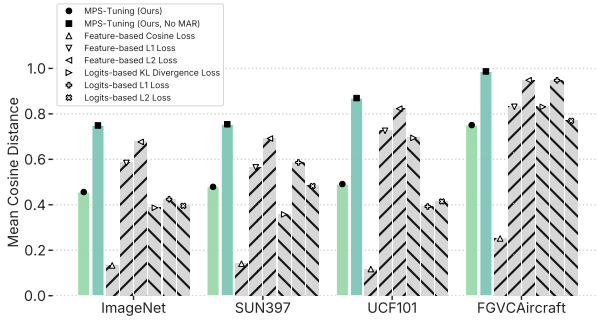


Figure 8: Cosine-Based Quantification of Feature Shift Induced by Diverse Consistency Constraints. A lower score indicates a stricter constraint on the output features.

tion when these hyperparameters were adjusted around their default values, demonstrating the robustness of our method to hyperparameter choices.

## G. More Interpretation Results

### Impact of Consistency Constraints on Model Adaptation

To substantiate the potential limitations of different consistency constraints discussed in the interpretability section of the main text, we conducted quantitative experiments analyzing changes in feature representations and logits distributions before and after fine-tuning.

**1. Feature-Level Analysis** We evaluated the cosine distance between model output features before and after fine-tuning across multiple datasets. In CLIP’s normalized feature space used for similarity computation, the difference between two vectors is measured by their angular separation. Since angular alignment is equivalent to vector alignment in this context, a larger cosine distance between pre- and post-fine-tuning vectors indicates greater overall divergence. As shown in Fig. 8, cosine similarity constraints result in minimal angular changes between pre- and post-fine-tuning models, even in cross-domain scenarios (e.g., FGV-

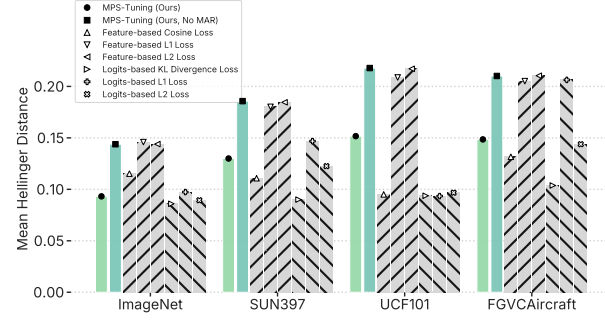


Figure 9: Hellinger-Based Metric for Quantifying Logits Shift Across Consistency Constraints. A lower score indicates a stricter constraint on the predicted outcomes.

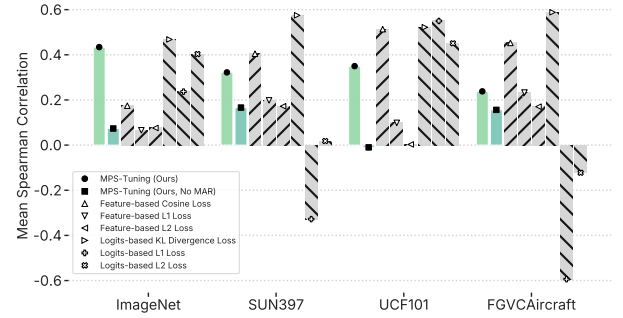


Figure 10: Spearman-Based Metric for Quantifying Logits Shift Across Consistency Constraints. A higher score indicates a stricter constraint on the predicted outcomes.

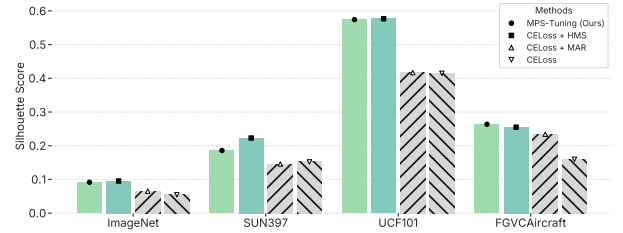


Figure 11: Impact of MAR and HMS on Feature Discrimination using Silhouette Coefficient. A higher score indicates better clustering performance.

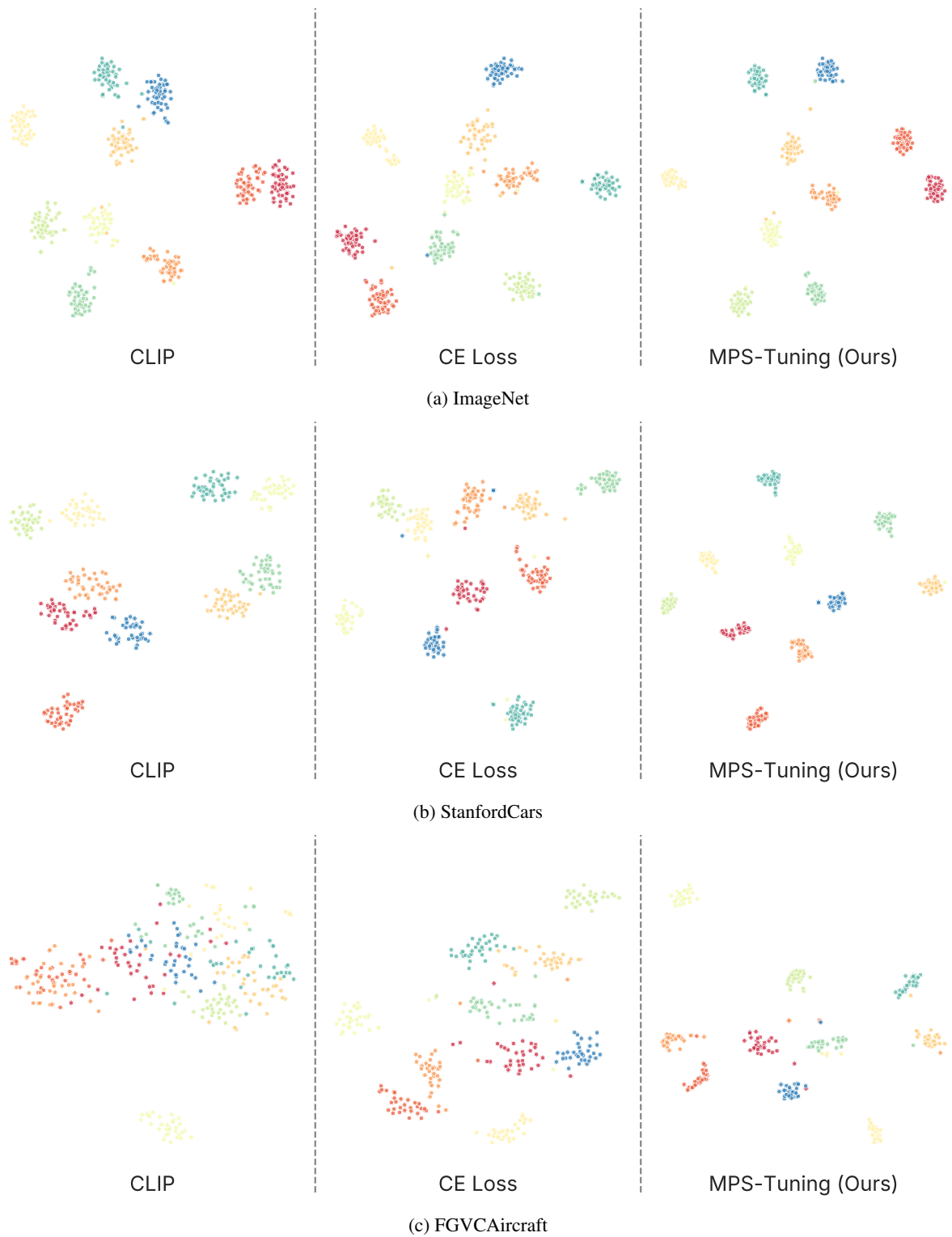


Figure 12: The t-SNE visualization, with each color denoting a distinct class.

CAircraft, where models typically require substantial adjustments for effective downstream task adaptation). This demonstrates that cosine similarity imposes more stringent restrictions on feature variations compared to other feature-based constraints.

**2. Logits-Level Analysis** We assessed the variation in prediction probabilities using Hellinger Distance and the consistency of prediction rankings via Spearman’s Rank Correlation, comparing models before and after fine-tuning. The former quantifies differences between two probability distributions, while the latter assesses the extent to which fine-tuned models maintain prediction ranking consistency with original models. The experimental results documented in Fig. 9 and Fig. 10 show that models constrained by feature-level cosine similarity and logits-level KL divergence demonstrate markedly superior alignment with original model predictions compared to their L1 and L2 constrained counterparts. This superiority manifests through consistently reduced Hellinger Distance values and elevated Spearman’s Rank Correlation coefficients, with the most pronounced differentiation occurring on the cross-domain FGVCAircraft dataset. These results confirm that cosine similarity and KL divergence heavily constrain model predictions.

These findings indicate that cosine similarity and KL divergence may impose overly rigid constraints, potentially hampering the model’s learning capacity. In contrast, our proposed Manifold Alignment Regularization (MAR) offers a dynamic constraint mechanism that adapts across datasets, enabling models to engage in further learning when knowledge acquisition is necessary while effectively preserving pre-trained knowledge when high consistency exists between pre-trained and downstream task-required knowledge, thereby significantly enhancing model learning capability.

### **Impact of MAR and HMS on Feature Discrimination**

We further employed a common clustering metric, the Silhouette Coefficient, to evaluate the class separability of features in the representation space across different model components. As shown in Fig. 11, using MAR alone improves class separability in certain scenarios, while HMS alone significantly enhances the distinction between categories. The combined use of MAR and HMS yields results comparable to using HMS alone, indicating the effectiveness of our approach in facilitating discriminative feature learning.

## **H. Visualization**

We visualize the features using t-SNE on the ImageNet, StanfordCars, and FGVCAircraft datasets under the 16-shot setting. As illustrated in Fig. 12, MPS-Tuning yields superior intra-class compactness and inter-class separability compared to both the non-fine-tuned model and Cross-Entropy loss (CEloss) fine-tuning. Notably, in scenarios where the original CLIP model performs well (e.g., ImageNet and StanfordCars), MPS-Tuning more effectively preserves the original semantic structure and inter-class relationships than CE loss tuning. In contrast, for datasets where

CLIP underperforms (e.g., FGVCAircraft), the global semantic structure is largely retained, while local adjustments facilitate improved classification.